Deciphering Epiphreatic Conduit Geometry from Head and Flow Data

8

Matej Blatnik, David C. Culver, Franci Gabrovšek, Martin Knez, Blaž Kogovšek, Janja Kogovšek, Hong Liu, Cyril Mayaud, Andrej Mihevc, Janez Mulec, Magdalena Năpăruş-Aljančič, Bojan Otoničar, Metka Petrič, Tanja Pipan, Mitja Prelovšek, Nataša Ravbar, Trevor Shaw, Tadej Slabe, Stanka Šebela, and Nadja Zupan Hajna

Karst aquifers are hydraulic structures where dissolution conduits dictate complex spatial and temporal flow patterns. These aquifers are vertically divided into phreatic, epiphreatic and vadose zones. While the phreatic zone is permanently saturated, providing the major contribution to base flow, most of the flood event water is transferred through the epiphreatic zone. The spatial distribution of conduits within karst aquifers is largely unknown. The only technique giving accurate results is direct human exploration, although some limited information can be obtained from hydrograph analyses in springs and wells, through hydraulic tomography and by geophysical surveys.

Providing that the structure and boundary conditions stay constant, karst aquifers are driven toward equilibrium, where conduit systems effectively drain all of the available recharge. Many karst areas are within young orogens, where the evolution of conduits has been affected by continuous changes in base level and structure (Gabrovšek et al. 2014; Audra and Palmer 2013). Such evolution results in a complex system of conduits across multiple levels. Conduit networks in active tectonic settings typically have extremely variable geometry, with high variations of conduit cross-sections and termination of conduits by breakdown or fault planes. This results in such systems being permanently out of equilibrium, and gives rise to high water level variations.

M. Blatnik · F. Gabrovšek · M. Knez (✉) · B. Kogovšek · J. Kogovšek · C. Mayaud · A. Mihevc · J. Mulec · M. Năpăruş-Aljančič · B. Otoničar · M. Petrič · T. Pipan · M. Prelovšek · N. Ravbar · T. Shaw · T. Slabe · S. Šebela · N. Zupan Hajna
Research Centre of the Slovenian Academy of Sciences and Arts, Karst Research Institute, Postojna, Slovenia
e-mail: knez@zrc-sazu.si

D. C. Culver
American University, Washington, DC, USA

H. Liu
Yunnan University, Kunming, China

The epiphreatic zone (EZ) (Fig. 8.1) transfers most of the floodwater and enables fast transport of pollutants. Groundwater dynamics in the EZ can be observed by setting up networks of autonomous sensors/loggers in the epiphreatic caves. These loggers record groundwater levels, temperature, specific electric conductivity and other physicochemical parameters. Such monitoring has proven to be a valuable approach; however, the data interpretation is still under development. When basic characteristics of input/output relations are questioned, typical methods of time-series-analyses can be used to extract lumped parameters of the system.

The main objectives of monitoring and data analysis in epiphreatic zone are

- to obtain information on the unknown geometry of the system based on the hydrographs,
- to relate observed hydrographs to the known geometry and characteristics of recharge.

It has been demonstrated that a careful analysis of recorded hydrographs combined with numerical models could result in a wealth of such information (Chen and Goldscheider 2014; Jeannin 2001; Peterson and Wicks 2006; Gabrovšek and Peric 2006; Gabrovšek et al. 2018; Kaufmann et al. 2016; Vuilleumier 2019). In this chapter, we review some of the principles and give two examples from the Slovene Dinaric karst.

8.1 Theoretical Background

8.1.1 Flow Regimes in the Epiphreatic Zone

Flow in karst aquifers occurs in all possible regimes: free surface and pressurized conduit flow, laminar flow in fractures, free film flow on the walls, and diffuse (Darcy) flow in porous medium (Ford and Williams 2007). Exchange flow between different porosity types brings further complication.

M. Knez et al. (eds.), *Karstology in the Classical Karst*, Advances in Karst Science,
https://doi.org/10.1007/978-3-030-26827-5_8

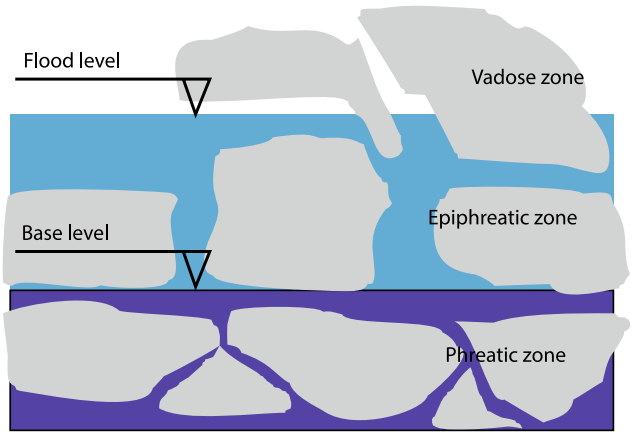

Fig. 8.1 A simple vertical section through a karst aquifer

When analysing flood response in mature, conduit dominated karst aquifers, turbulent flow in open and pressurized conduit networks needs to be considered.

8.1.1.1 Saint-Venant Equation of Open Channel Flow

One-dimensional, transient, free surface flow in open channels is described by the Saint-Venant equations, which are derived from mass and momentum conservation over the entire flow cross-section. Derivation is based on small streamline curvature, no vertical acceleration (uniform velocity across the vertical profile) and small bed slope Θ (i.e. $\sin(\Theta) = \Theta = i$). We give a brief outline of the derivation.

Figure 8.2 shows a section of a channel with length dx. A difference between the inflow and the outflow from the section equals the rate of change of storage (i.e. volume) within the section. If q (m^2/s) is lateral inflow per unit length, it has to be added to the mass conservation, which then requires

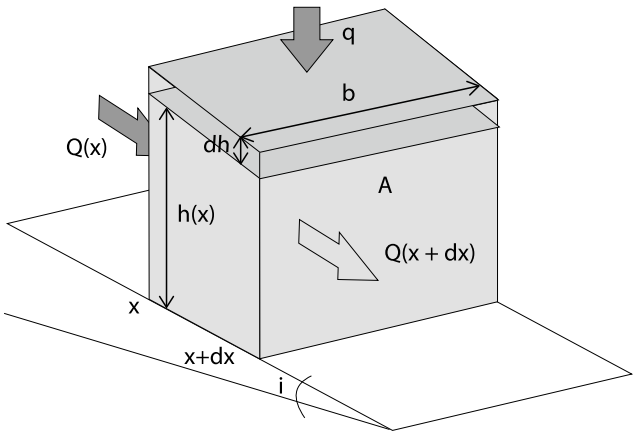

Fig. 8.2 Conservation of flow in a differential stream section gives one of the Saint-Venant equations

$$b(h)\frac{\partial h}{\partial t} + \frac{\partial Q}{\partial x} = q \tag{8.1}$$

As seen from Fig. 8.2, A is the cross-sectional area of the flow, b is width of the flow at the water surface, h is the depth of the flow and Q is the flow rate. Applying $Q = A \cdot v$, where v is the flow velocity, Eq. 8.1 becomes

$$b(h)\frac{\partial h}{\partial t} + A\frac{\partial v}{\partial x} + v\frac{\partial A}{\partial x} = q \tag{8.2}$$

The second Saint-Venant equation is derived from Newton's second law. The rate of change of momentum in the section equals to the sum of the difference between the momentum rate entering and exiting the section, and all the external forces acting on it. This can be written as

$$\frac{\partial v}{\partial t} = \frac{1}{\rho A dx}\sum F_{ext} - v\frac{\partial v}{\partial x} + qv_x \tag{8.3}$$

where the first part on the right-hand side presents external forces, the second part the change of momentum rate entering and exiting the section at x and $x + dx$, respectively, and the third part the momentum rate of the lateral inflow in direction x.

In a natural setting three types of forces act on the fluid parcel: the gravitational force, the force of the static pressure change and frictional forces. For small slopes $(\sin(\Theta) = \Theta = i)$, these become

$$\begin{aligned} F_{g,x} &= \rho g A i dx \\ \mathrm{F_p} &= -\rho g A i \frac{\partial h}{\partial x} dx. \\ F_f &= -\rho g A j dx \end{aligned} \tag{8.4}$$

where $F_{g,x}$ is gravitational force, F_p pressure force and F_f frictional force in the flow direction x, where j is frictional energy gradient, ρ is the density of water and g is gravitational acceleration.

Combining Eqs. 8.3 and 8.4 gives the momentum part of Saint-Venant equation:

$$\frac{\partial v}{\partial t} + v\frac{\partial v}{\partial x} + g\frac{\partial h}{\partial x} = g(i - j) + qv_x \tag{8.5}$$

Equations 8.2 and 8.5 give the set of Saint-Venant equations. Further details on the equation can be found in classical textbooks (Chow 1988; Dingman 2002). There is no analytical solution for the complete set of Saint-Venant equations, but many numerical approaches exist.

Several empirical relations are used to calculate the friction slope. A common choice is the Manning formula

$$j = \frac{n^2 Q^2}{A^2 R^{4/3}} \tag{8.6}$$

where n is Manning's (empirical) roughness coefficient (the roughness of natural underground channels occupies a large span of values between 0.03 and 0.15), A is the area of flow cross-section and R the hydraulic radius, the ratio between the area and the wetted perimeter.

Under certain conditions, some terms in Eq. 8.5 can be neglected. Kinematic approximation neglects pressure forces and acceleration terms, which represent the entire left-hand side of Eq. 8.5. With no lateral input, Eq. 8.5 reduces to $i - j = 0$, i.e. the friction slope equals the bed slope. In a uniform channel, the result of the kinematic approximation is a flood-wave, which travels downstream unaltered with a velocity $3U_u/2$, where U_u is velocity obtained from Manning formula. A closer approximation is a Convection–Diffusion Equation, which keeps the pressure forces $g \cdot \partial h/\partial x$, but neglects the inertial forces. The result is a flood-wave with declining crest as it moves downstream. The equation also accounts for the backwater effects.

The most radical approximation of the Saint-Venant equation is a steady state one, which then reduces to a friction slope equation, such as the Manning equation (Eq. 8.6).

8.1.1.2 Steady-State Equations for Open Channel and Pressurized Flow

Underground rivers experience transitions to pressurized (full pipe) flow. In open channel (free surface) flow, the relation between discharge and slope depends on the hydraulic radius and flow cross-section. Rozos and Koutsoyiannis (2006) modified the Manning formula to account for the steady-state free surface and pressurized flow:

$$Q = \frac{\beta}{n}\left(\frac{h}{D}\right)^{\alpha} i^{1/2} \tag{8.7}$$

where D is the maximal depth of a conduit, β and α are constants depending on the cross-sectional geometry. Rozos and Koutsoyiannis (2006) numerically tested a number of cross-sections and got $\alpha = 2$ for circular and $1 < \alpha < 5/3$ for rectangular cross-sections with width to height ratio between 0 and ∞. Inverting Eq. 8.7, we get $h \propto Q^{1/\alpha}$ for an open channel, where $\alpha \geq 1$ for most cross-sections. Therefore, the $h(Q)$ *term* follows a sublinear regime. Intuitively, in the open channel, the increase of flow is compensated for by an increase of depth and flow cross-section, which results in the sublinear relation between flow depth and flow rate. In a pressurized conduit, $h/D = 1$, and the head required to drive flow through the channel rises as $\Delta h \propto Q^2$.

To demonstrate the above reasoning, Fig. 8.3 shows the water depth measured at the entrance to a 200 m long circular conduit with a diameter of 1.5 m, when the flow rate slowly increases from 0 to 8 m^3/s. Initially $Q(h)$ follows a square root relation, which changes to a cubic relation when the conduit becomes pressurized ($h = D$). The red line shows the $h(Q)$ relation within the channel. The small inserts show the concept. Note that for the full pipe regime, h is the head required to drive the flow rate Q through the conduit.

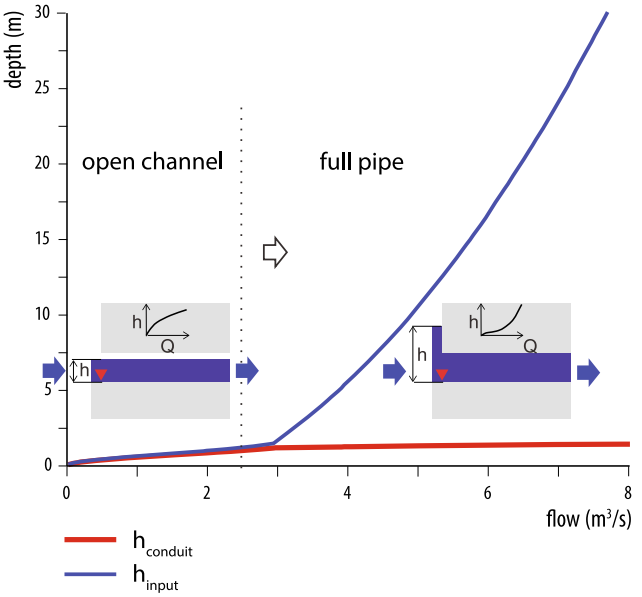

Fig. 8.3 Dependence of water depth at the input junction (head, h) on the flow rate (blue line) and inside (red line) a 200 m long circular conduit with diameter 1.5 m; roughness factor is 0.05

Typical measurement sites in cave streams involve pools and riverbeds in open channels. Pressure transducers record the actual pressure at the site, which is a sum of the barometric (air) pressure, static water pressure $(\rho \cdot g \cdot h)$, and the

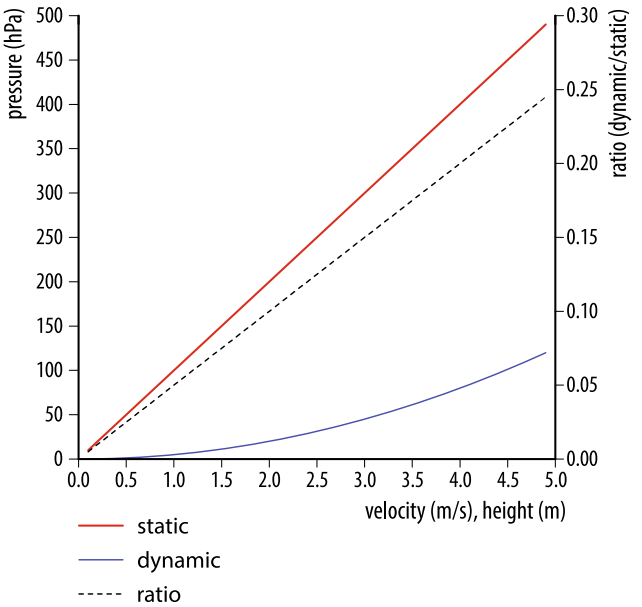

Fig. 8.4 Relation between static pressure to water depth (red line) and dynamic pressure to water velocity (blue line)

dynamic water pressure $(0.5 \cdot \rho \cdot v^2)$, where v is the water velocity (Fig. 8.4). One should have this in mind when translating data into height and when positioning the instruments. They should not be placed at positions with high velocity and low height, such as in the regions of supercritical flow. Note that barometric pressure must be subtracted in order to get correct water depth, or a vented transducer must be used.

8.2 Modelling Flow in the Epiphreatic Zone

8.2.1 EPA Storm Water Management Model

In this chapter, we simulate flow in conduits with the Storm Water Management Model (SWMM), developed by the US Environmental Protection Agency (EPA 2014). SWMM is an efficient, versatile and open environment, which solves full or approximated Saint-Venant equations in arbitrary network of conduits and channels. SWMM was primarily developed to simulate urban sewage systems, but has found many implications in the study of karst conduit networks (Chen and Goldscheider 2014; Kaufmann et al. 2016; Peterson and Wicks 2006). The model allows the simulation of various possible scenarios and permits the use of many elements of man-made and natural hydraulic systems. To account for the transition from an open channel to full pipe flow, a surcharge algorithm is used (Rossman 2009). In this work, we used the full dynamical wave solution for calculations.

One can choose between a variety of predefined and user-specified channel cross-sections, and can also define channel dimensions. A Manning's roughness coefficient is assigned to each channel; here an empirical value for stony channels with cobbles $n = 0.035$ was used. Figure 8.5 shows elements of the SWMM model used in this work in cross-section (a) and 3D view (b). Each channel/conduit is connected to two nodes with a given invert elevation, maximal and surcharge depths. A channel can enter a node at a particular offset above the invert elevation. Nodes can be converted to storage units, to which a power law or tabular curve is used to consider the dependence of surface area on the water level. Nodes can also be outlets (spring) or flow dividers. A constant value time series of recharge can be assigned to any node.

A typical situation in the epiphreatic zone occurs when the rising water reaches the overlying conduit, which then effectively drains the water under free surface flow conditions. The concept is shown on Fig. 8.6. There, the depth is recorded in a chamber drained by conduits C_1 and C_2 at different elevations (red triangle). With increasing recharge flow in C_1, the system undergoes transition from free surface to pressurized flow. When water reaches conduit C_2, the story repeats; initially C_2 drains water with a free surface, but if the recharge still increases C_2 also becomes pressurized, resulting in a fast increase of depth. The graph on the right shows an idealized relation between the depth and the recharge, with inflections denoting the transitions of flow regime in C_1 and C_2.

The reasoning given above demonstrates that a careful hydrograph analysis can reveal the existence and positions of unknown overflow levels and can therefore improve the knowledge of aquifer geometry. In the following section, we explore numerically, where and under what conditions, how such overflows can be detected by observations.

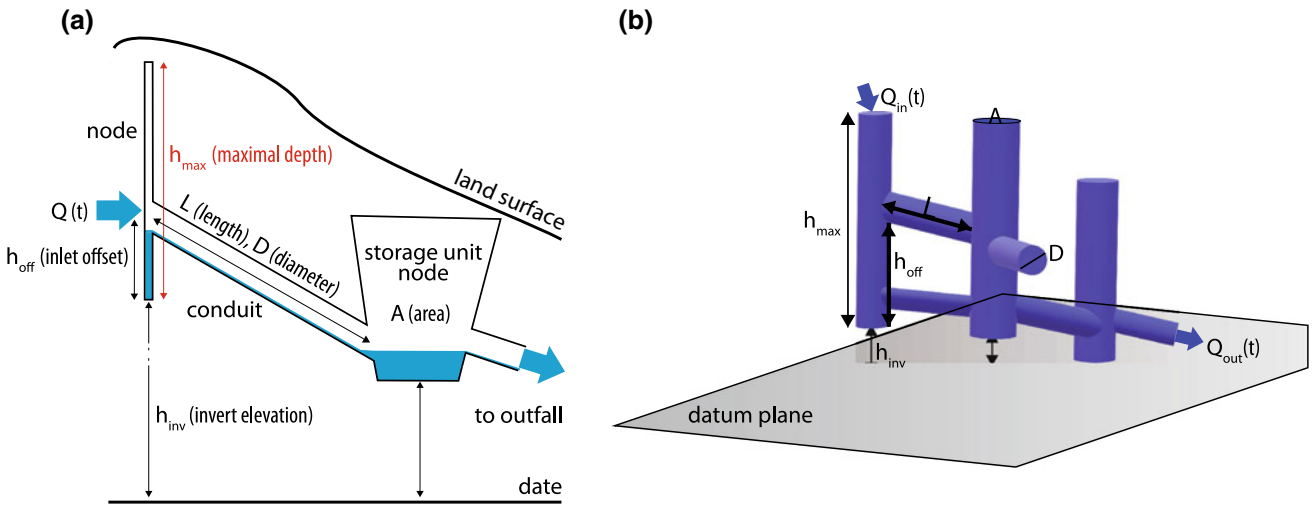

Fig. 8.5 **a** Cross-section and **b** 3D views of the key elements of SWMM models used in this work

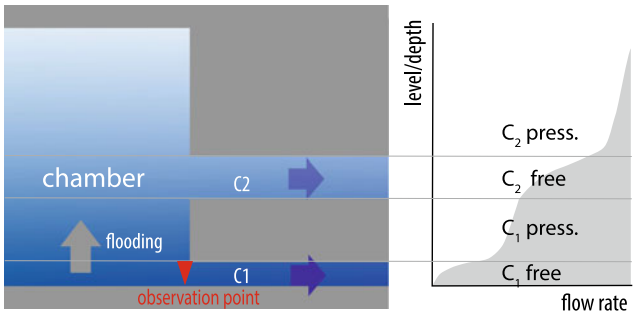

Fig. 8.6 Concept of overflow detection. Inflections on a level hydrograph (right) caused by transitions between open channel and pressurized flow regimes occurring at the same levels during different events may indicate the presence of overflow routing. Blue arrows indicate flow direction, a grey arrow indicates flooding. The shape of the curve under free surface condition corresponds to a circular tube

8.2.2 Modelling Overflows in the Epiphreatic Zone

8.2.2.1 A Single Overflow

As a basic building block, a single overflow passage between two observation points is shown in Fig. 8.7. The overflow can either span the entire distance between the two points (Fig. 8.7a) or can only shortcut the distance partially (Fig. 8.7b).

The question is when and how can the overflow be "seen" from the level hydrographs at points P_1 and/or P_2.

It is beyond the scope of this work to discuss the entire range of parameters. We present here only some typical representative cases, and summarize the possible outcomes. The models were composed by implementing the previously discussed equations within SWMM. The varying parameters are the diameters of base flow conduits, D_1 and D_2 for a single overflow and D_1–D_3 for two overflows. All other parameters are kept constant if not stated otherwise.

Figure 8.8a shows the case where $D_2 \gg D_1$, so that the water at P_2 can freely flow out from the system, without raising the level at P_2 to the position of the overflow. The level hydrograph at P_1 (solid red line) has two inflections, one each at the rising and recession stages, at the position of the overflow conduit (h_O = 20 m). The opposite order of events happens during recession. The overflow is clearly visible from the hydrograph at P_1. At P_2 the overflow is not detected. The red dashed line shows the case where the overflow channel is large enough to accommodate all of the flow without becoming pressurized. In such a case, the overflow position represents peak head for a wide range of events.

In Fig. 8.8b the opposite case is shown where D_2 is restrictive, i.e. $D_2 \ll D_1$. The levels at P_1 and P_2 are entirely controlled by D_2, making h_1 and h_2 almost the same. The overflow is back-flooded and therefore not visible on both hydrographs.

In a third scenario (Fig. 8.8c, d) D_1 and D_2 are comparable, so that the level at P_1 is always distinctively higher than the level at P_2, and the level at P_2 rises above the overflow position. Initially both levels increase simultaneously following the free surface flow rules. To conclude, an overflow level can be recognized from a depth/level hydrograph if the overflow is down-flow from the observation point and that the back-flooding is a not dominant reason for the head increase at the point. In other words, overflow must shortcut a considerable head difference.

8.2.2.2 A Series of Overflows

Real systems are usually more complex, so one may expect a series of overflows (Fig. 8.9).

All findings for a single overflow are valid for P_1, except in the case when h_{o1} is close to h_{o2}, where O_2 masks the record of O_1. If the vertical distance between the overflows is sufficient, two distinct inflections are seen at P_1, presenting

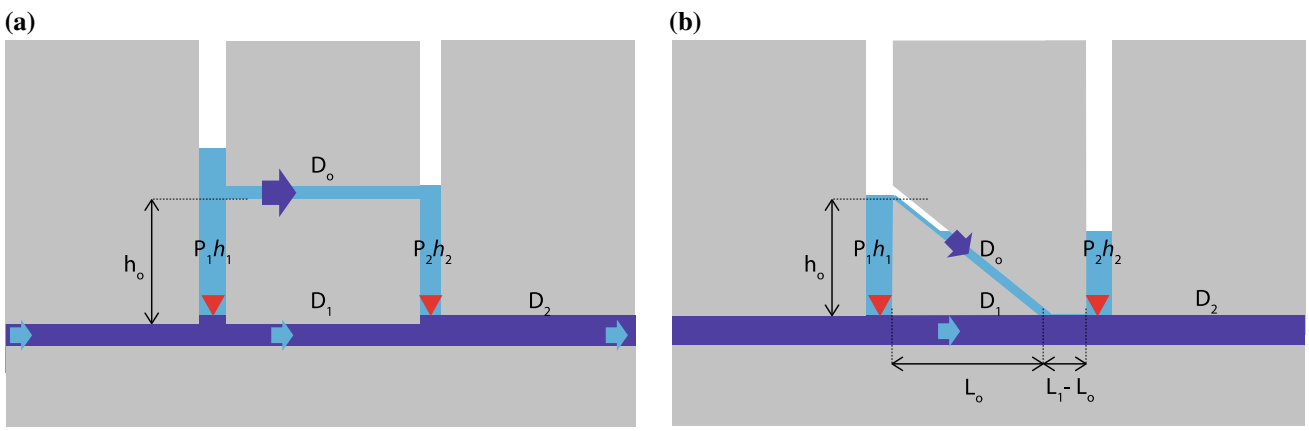

Fig. 8.7 Conceptual cross-sectional diagram of a single overflow connecting observation points P_1 and P_2. **a** Horizontal overflow channel spanning the entire distance between P_1 and P_2; **b** an inclined overflow channel, shortcutting only part of the distance between P_1 and P_2

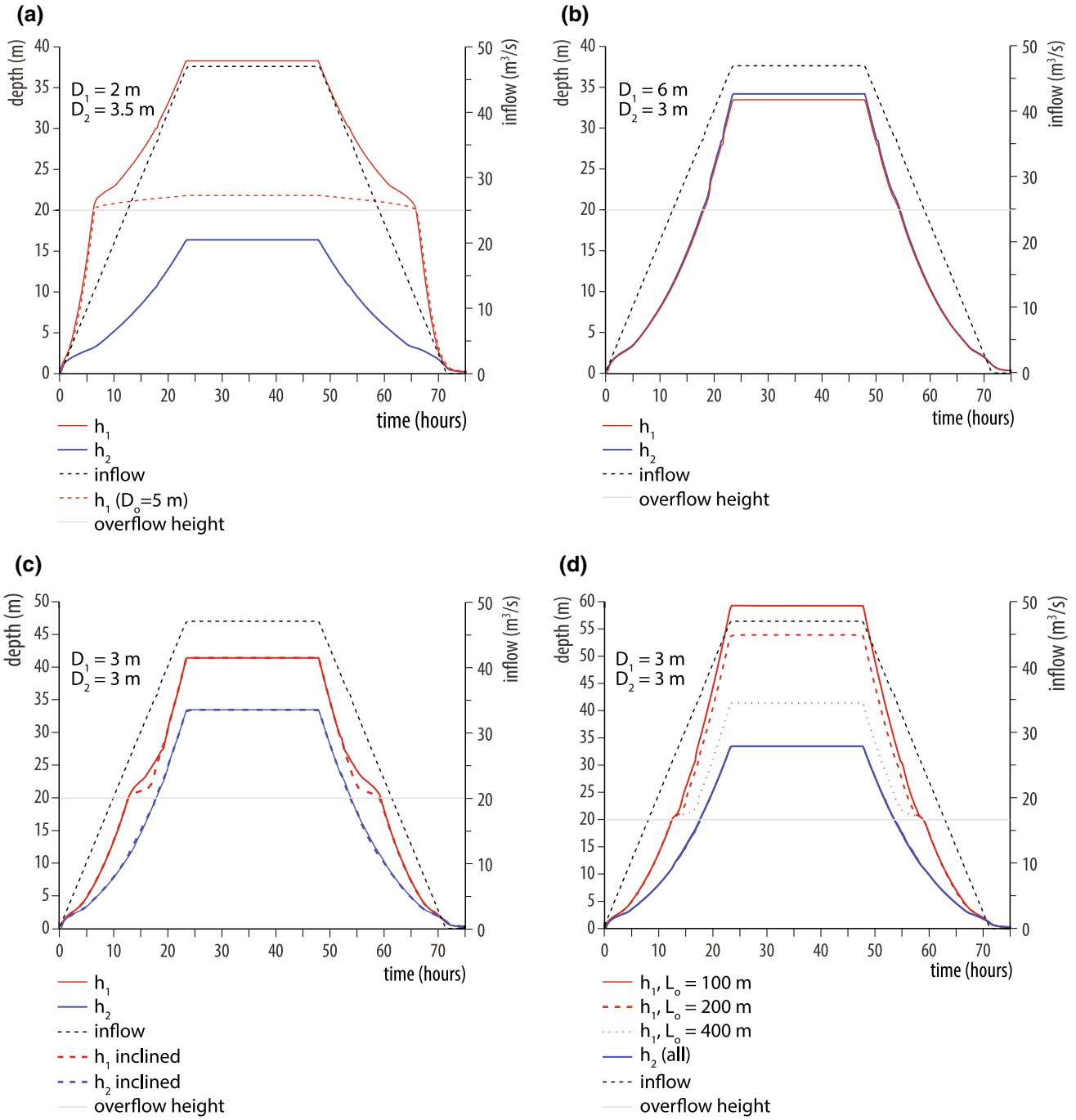

Fig. 8.8 Theoretical depth/level hydrographs for a 75 h flood event at points P_1 and P_2 (see Fig. 8.7). The dotted line shows the position of the overflow. **a** $D_2 \gg D_1$, **b** $D_1 \gg D_2$, **c** $D_1 = D_2$, **d** $D_1 = D_2$, for partial overflow (Fig. 8.7b)

O_1 and O_2, respectively (Fig. 8.9a). As there is a head difference between P_1 and P_2, the inflection at P_1 is higher than the actual position of overflow O_2. In the case shown in Fig. 8.9c (restrictive D_2), overflow O_1 is back-flooded and only O_2 is seen at both observation points. By adding further complexity, multiple situations could be obtained, but as a general rule we can say that at a certain observation point, downstream overflows are seen if the point is hydraulically connected to the overflows and if the overflows shortcut considerable head difference.

8.2.2.3 Three Overflows

The final example includes three overflows and three observation points (Fig. 8.10a). Figure 8.10a–e presents a

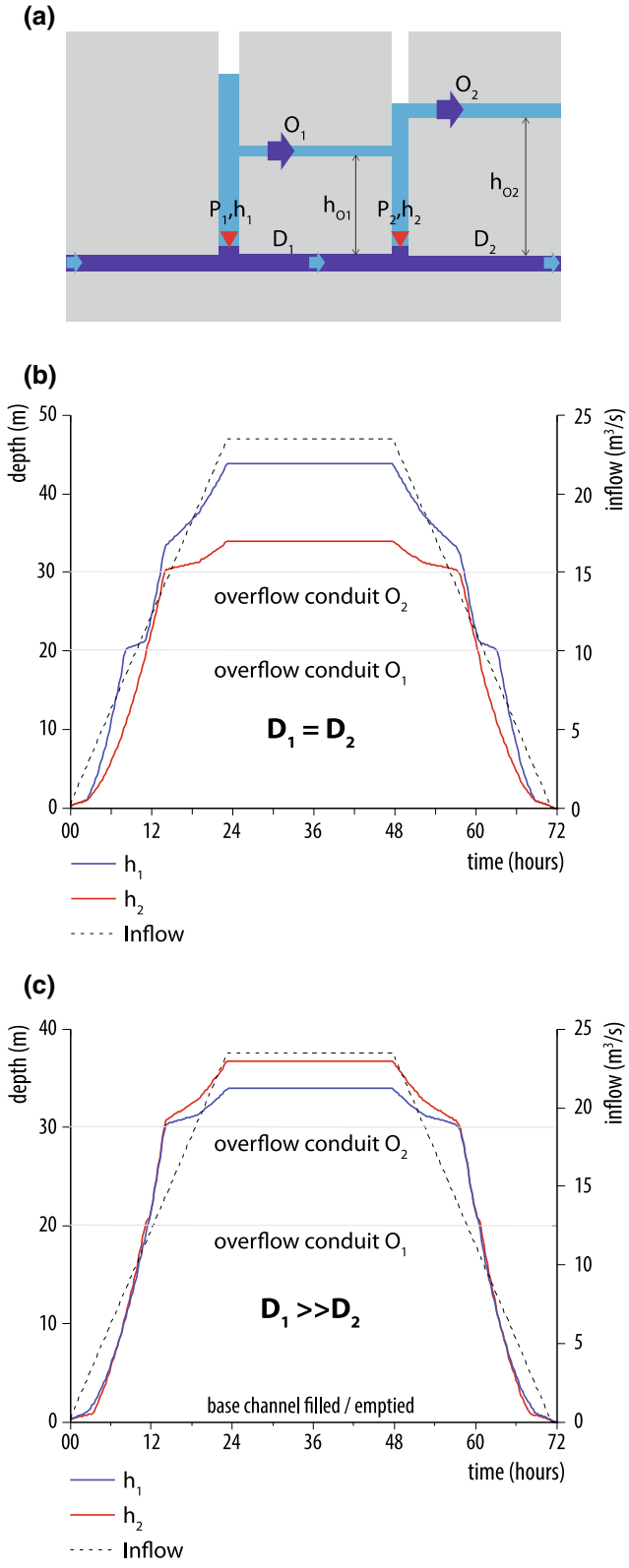

Fig. 8.9 **a** Conceptual cross-sectional diagram of two overflows in series, **b**, **c** hydrographs at P_1 and P_2 for two serial overflows, **b** $D_1 = D_2$, **c** $D_1 \gg D_2$

set of outcomes resulting from varying D_1, D_2 and D_3 and h_{O1}, h_{O2} and h_{O3}. Generally, the reasoning given for two overflows can be extended further, and a similar interplay between the position of overflow channels and size of the base channel results in multiple outcomes. With the reasoning given for single and two overflows, a reader can now easily understand the results and foresee settings that are even more complex.

8.3 Field Cases

To demonstrate some of the concepts and principles given above, we now present two cases from the Slovene Dinaric Karst. Two major flow systems are the Ljubljanica catchment area and the aquifer of the Kras Plateau. Autonomous observation of epiphreatic flow in both systems was started more than a decade ago, where long-term time series have been recorded and analysed. Detailed description of the work and results have been published in several papers (Gabrovšek and Peric 2006; Kaufmann et al. 2016; Gabrovšek et al. 2018; Blatnik et al. 2019).

8.3.1 The Aquifer of the Kras Plateau: Škocjan Caves and Kačna Cave

8.3.1.1 General Overview of the Area

The aquifer of Kras is roughly a 40 km long, 13 km wide and several kilometres thick carbonate slab, extending in a SE–NW direction between Škocjanske jame (Škocjan Caves), the Soča River, Vipava Valley and the Bay of Trieste (Fig. 8.11). It is surrounded by flysch areas, giving rise to magnificent contact karst features. The main allogenic input into the system is the Reka River, with long-term (1952–2013) average discharge of about 8 m^3/s (ARSO 2016). The ratio between the highest and the lowest flow rate in the period 2005–2013 was 1700, with a maximum measured discharge of 305 m^3/s and a minimum of 0.18 m^3/s.

8.3.1.2 The Upper Reka–Timavo System: Škocjan Caves and Kačna Cave

The Reka River enters the aquifer at Škocjan Caves (Škocjanske jame). Its flow can be currently reached in eight other caves between Škocjan Caves and a series of springs between Aurisina and Duino at the NW coast of the Trieste Bay, with the Springs of Timavo being the most abundant (Fig. 8.11). The data, interpretation and modelling are presented by Gabrovšek et al. (2018).

Here we focus on the first part of the system, Škocjan Caves and Kačna jama (Kačna (Snake's) Cave).

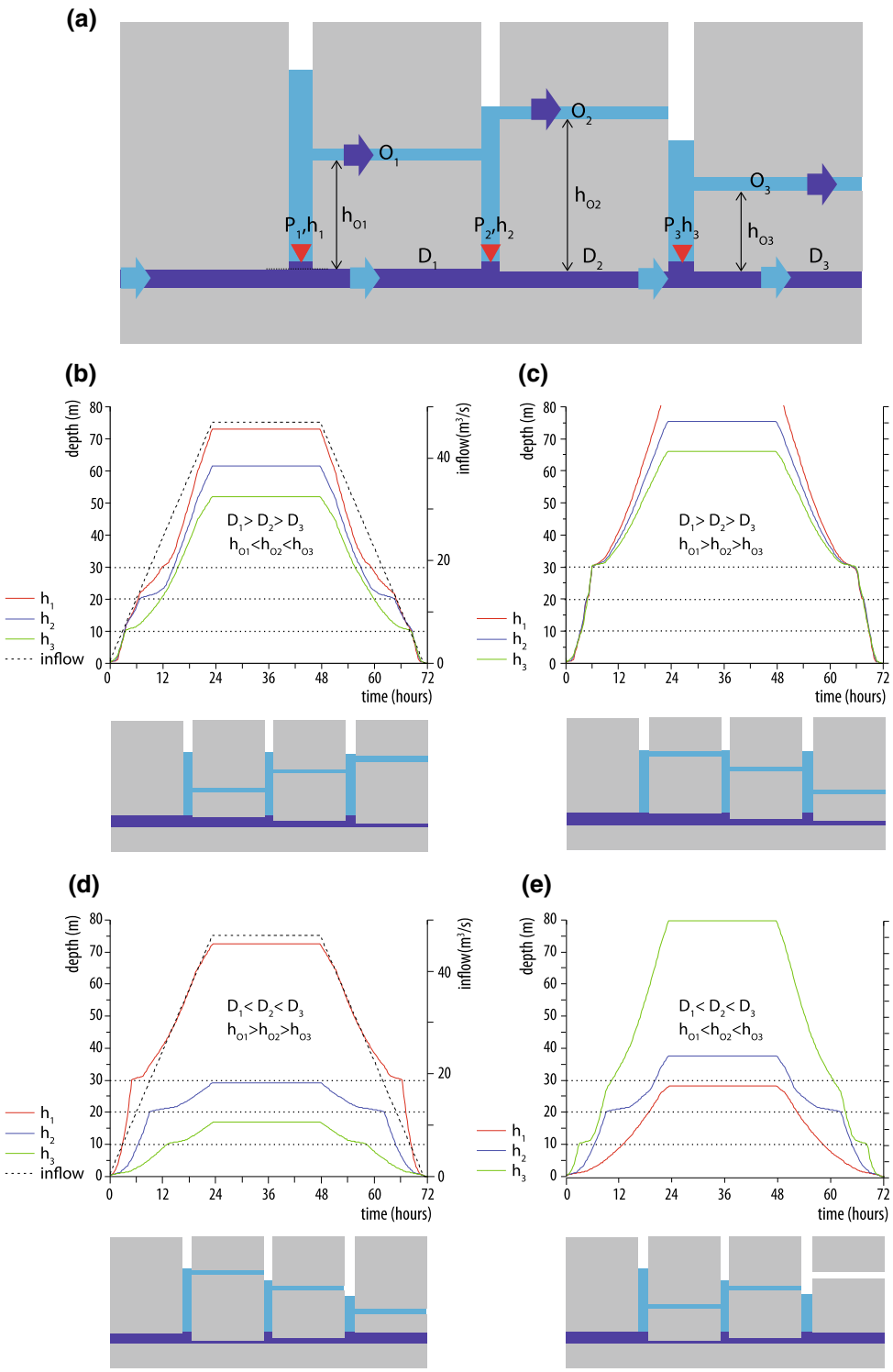

Fig. 8.10 Different scenarios with three observation points and overflows at different levels. Schemes below the graphs show the vertical distribution of overflows and diameters of base flow conduits. Dotted lines on the graphs show the position of overflows

The cross-section of this part is shown on Fig. 8.12. The Reka River reaches the flysch–limestone boundary about 7 km upstream from the Škocjan Caves and initially flows through a canyon. At the entrance to the Škocjan Caves, the canyon turns into an underground channel with a cross-section of 30 × 40 m, which is after few hundred metres interrupted by two large collapse dolines from where the river continues along an underground canyon; 2.6 km long, 10–60 m wide and 80–145 m high. The terminal part of the air-filled cave is Martel's chamber, with a volume of 2.6×10^6 m^3. There, the channel is interrupted by a cross-Dinaric fault (Šebela 2009), and the cross-sectional area drops abruptly by roughly three orders of magnitude, to "only" several tens of square metres. Here, at 214 m a.s.l., is

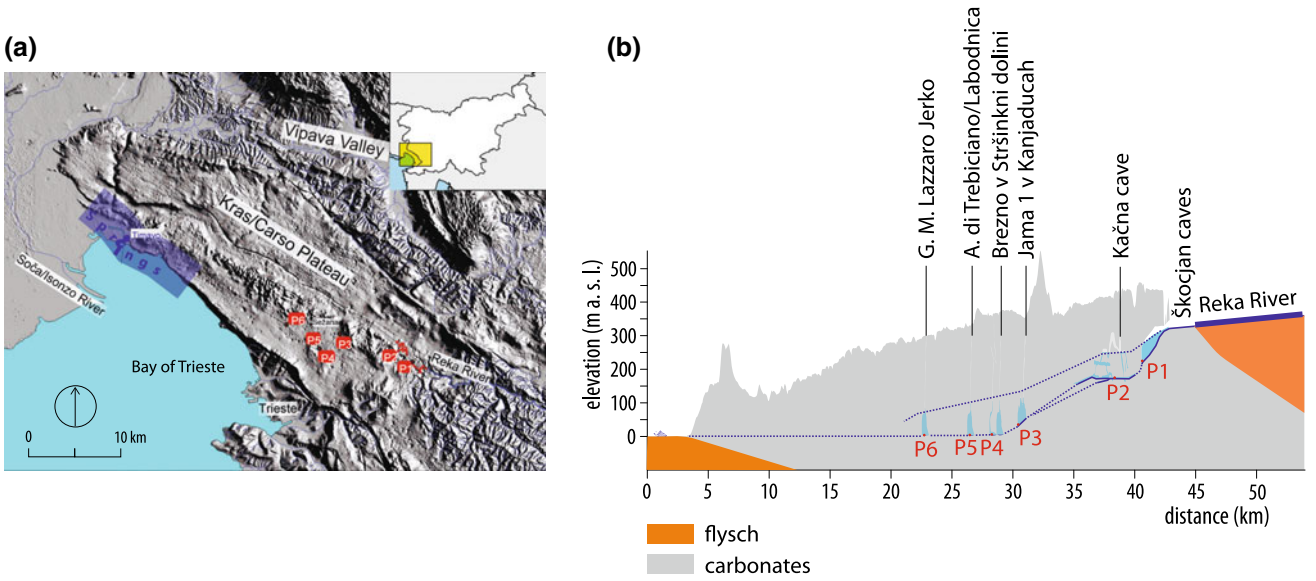

Fig. 8.11 **a** DEM terrain visualization and **b** topographic profile of the Kras/Carso Plateau with the position of some caves with access to groundwater flow. The dotted blue lines in the profile show base level and flood level at the observation points

the position of the first observation station P_1. From here, the flow follows a sequence of channels (with a cross-section of several tens of m^2) and continues into a sump, which is still unexplored, but the connection to another sump 800 m NW in the Kačna Cave is certain.

Kačna Cave can be entered from the surface through a 186 m deep shaft that connects to a complex system of epiphreatic and vadose channels, distributed along at least two distinct levels. The cave is more than 13 km long and 280 m deep. The lower epiphreatic level is dominated by the flow of the Reka River, which mostly flows in an open channel during low to medium hydrological conditions, when water leaves the cave through the terminal sump at 156 m a.s.l. Observation station P_2 in Kačna Cave is in the section called Brzice (= rapids) ~300 m upstream from the sump, at 175 m a.s.l. When the outflow capacity of the sump is exceeded, water flows along a system of overflow channels following the SE–NW (Dinaric) trend. More than 2 km of the overflow channels, interrupted by perched sumps, have been explored. Historical markings (organic debris) of floods in Kačna Cave are >100 m above the base flow level (Fig. 8.12).

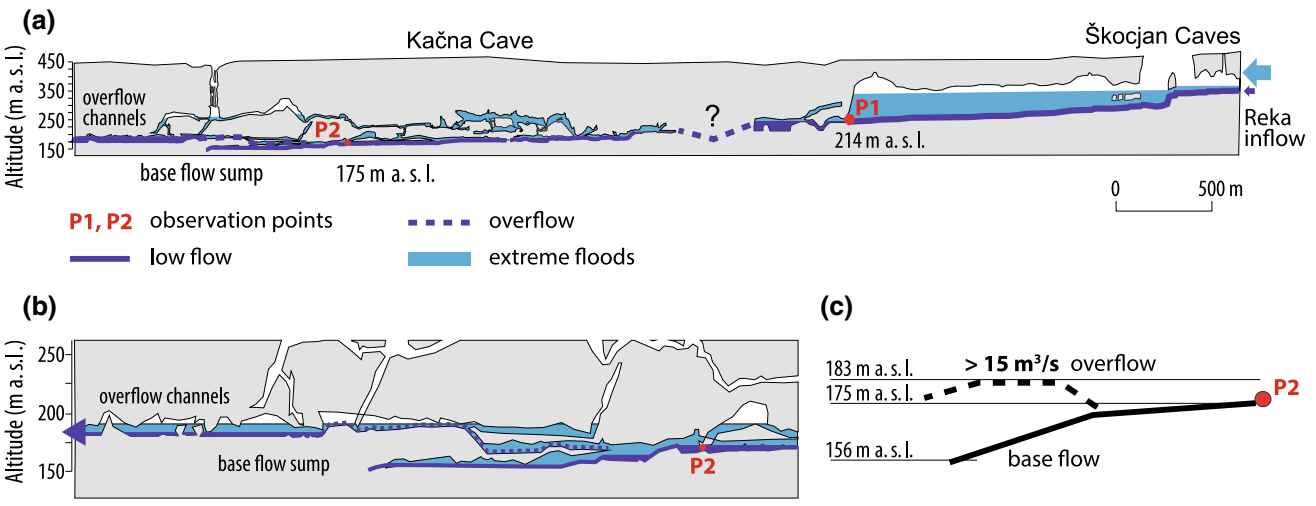

Fig. 8.12 **a** Cross-section through Škocjan Caves and Kačna Cave with the position of observation points P_1 and P_2. Dark blue lines/regions indicate low flow water positions, and the pale blue shows the floodwater situation; **b** detailed view of the region of P_2 in Kačna Cave; **c** flow routing at low flow (solid line) and high flow (dotted line) behind P_2

8.3.1.3 Flood Response

Figure 8.13 shows the response of the water level in Škocjan Caves (P_1) and Kačna Cave (P_2) during three events with different peak flows. During a small event, comparable responses at both locations are recorded (Q_{max} = 23 m^3/s, Fig. 8.13a). In a medium event (Q_{max} = 85 m^3/s, Fig. 8.13 b), the level at P_1 rises to 4 m, while the level at P_2 shows a steep rise to 15 m and slow recession (–2 m/day), as long as the flow rate is above 15 m^3/s. Finally, it recedes at the rate of about –4 m/day to the base level. During a large event (Q_{max} = 250 m^3/s, Fig. 8.13c) stage rises vigorously to 65 m at P_1 and 73 m at P_2, where it drops rapidly almost to the base level when the discharge drops below 100 m^3/s, while at P_2 stays elevated until Q > 15 m^3/s. During the rising stage of the medium and large events, inflection at about 13 m can be observed at P_2, suggesting an overflow level.

The situation is clearer in Fig. 8.14, which shows the level at P_1 and P_2 as a function of the Reka River flow rate for the entire observation period. For Q < 100 m^3/s, P_1 stays below 4 m, while the level at P_2 rises above 10 m for Q > 20 m^3/s. When flow is higher than 130 m^3/s, a steep rise with similar characteristics at both locations is observed.

The interpretation of the response and stage-discharge curves is given in Gabrovšek et al. (2018) and is based on the known geometry and base flow directions in Kačna Cave (see Fig. 8.12). There, the flow at low stage enters a narrow channel, which ends in a sump at 156 m a.s.l. The limited capacity of this outflow back-floods this part of the cave and diverts water into large galleries positioned about 9 m above the instrument. This obvious overflow resolves the first inflection in Kačna Cave (Fig. 8.13b, c).

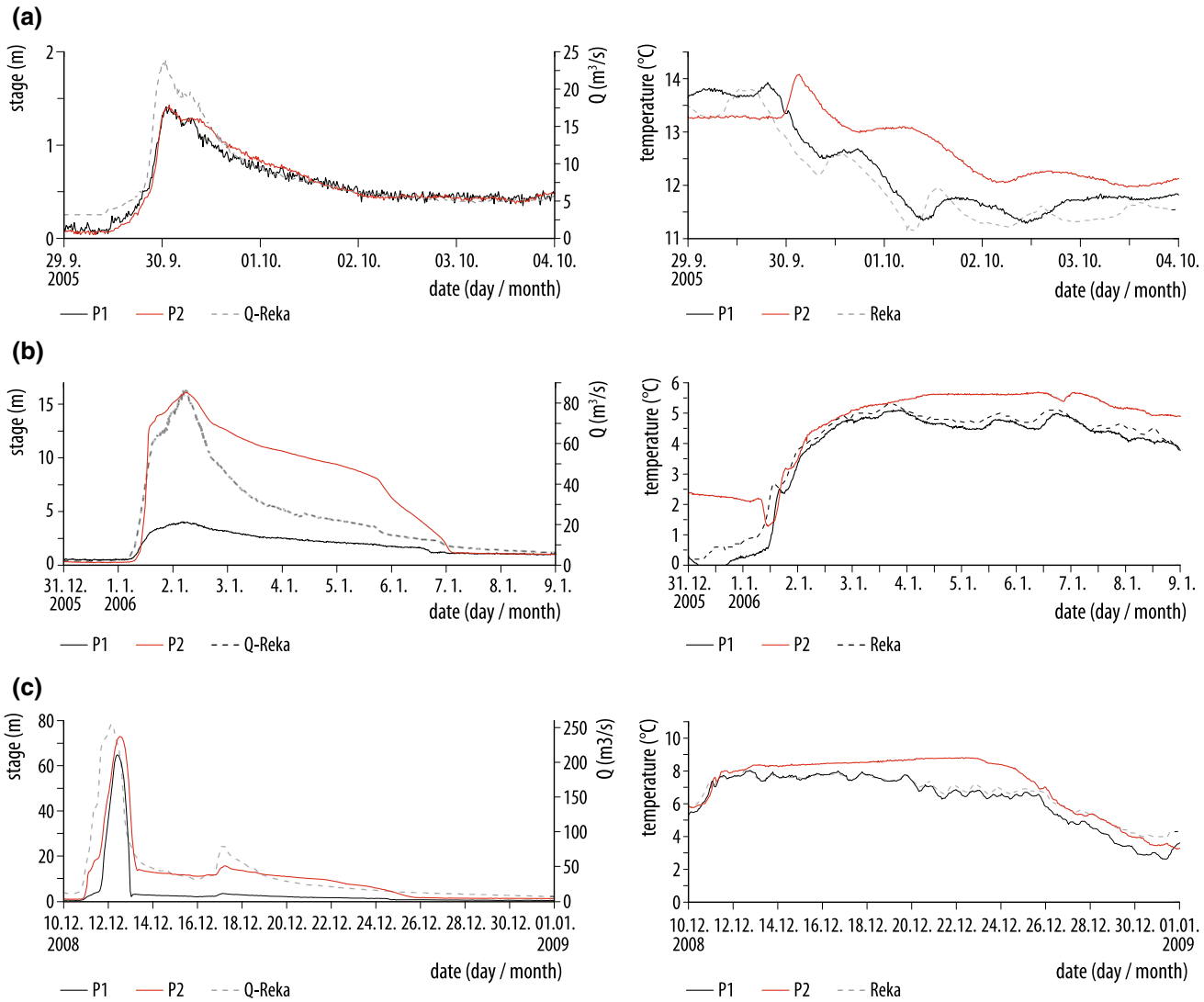

Fig. 8.13 Stage and temperature hydrographs at Škocjan Caves (P_1) and Kačna Cave (P_2) during **a** small, **b** medium and **c** large flood events. Note that the range of stage axis differs between the cases

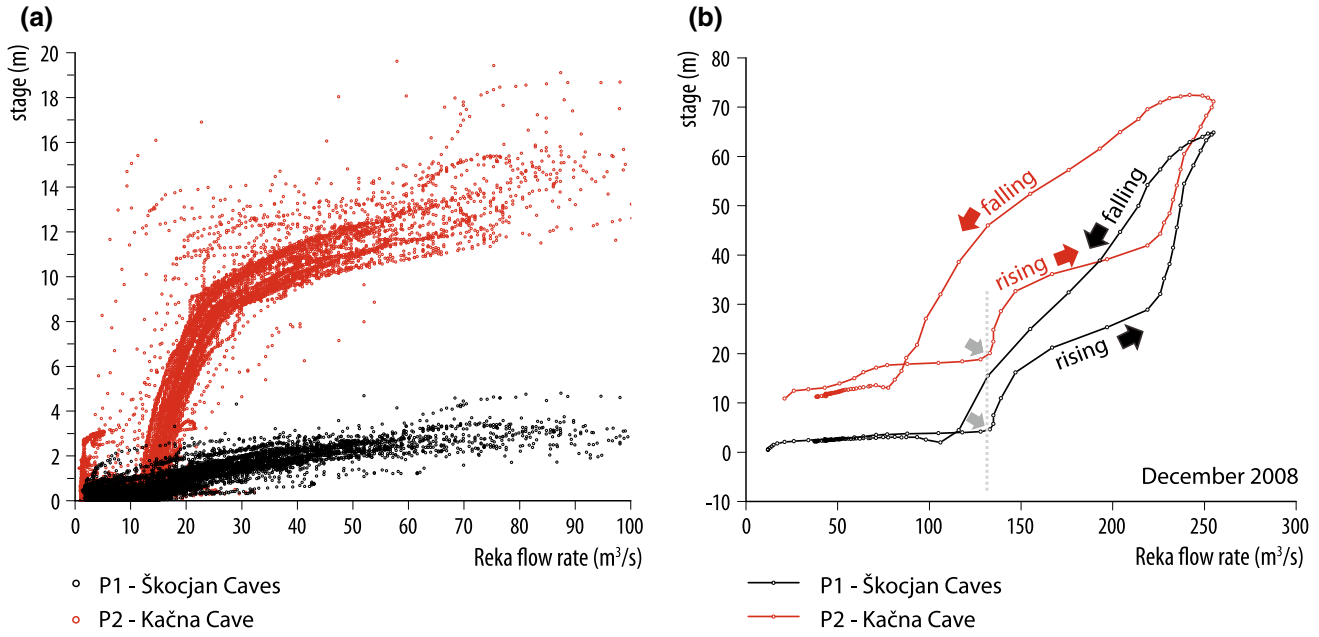

Fig. 8.14 Stage at P_1 and P_2 as a function of Reka River flow rate. **a** entire cloud of data points for $Q < 100$ m^3/s; **b** situation at a large flood event of December 2008. Note the common inflection towards steep rise at about 130 m^3/s, marked by grey arrows

However, a more interesting question is what causes large floods in Kačna Cave and particularly in Škocjan Caves, where the major inflection in the stage-discharge curve occurs at about 130 m^3/s (Fig. 8.14b). This inflection is *always* slightly preceded by a major inflection in Kačna Cave (grey arrows in Fig. 8.14b), which suggests that the back-flooding is triggered by the constriction behind the observation point in Kačna Cave.

Another insight is given by Fig. 8.15, which shows the relation between heads at both points. Two major floods from December 2008 and February 2009 deviate as large loops.

During the rising stages of both flood events, the heads at both caves start to correlate, when the head in Kačna Cave rises above 190 m a.s.l. Only a small deviation between both floods occurs during further increase (Fig. 8.15b). In general,

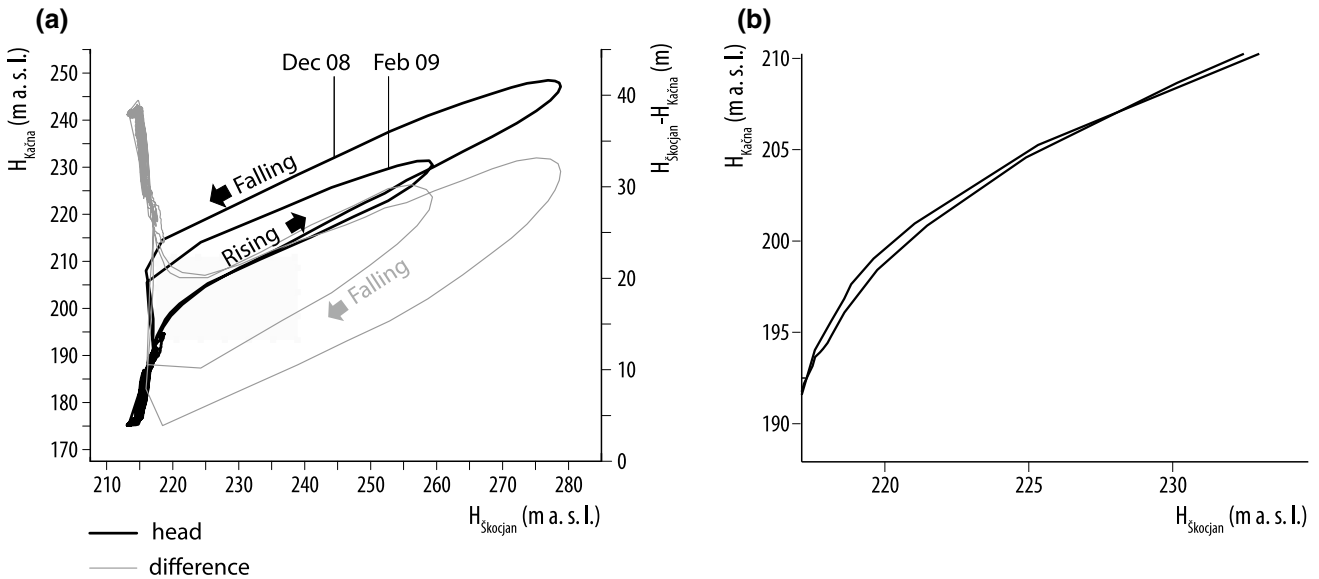

Fig. 8.15 **a** Black curve: the relation between heads in Škocjan Caves (P_1) and head in Kačna Cave (P_2). The grey curve shows difference $H_{Škocjan}–H_{Kačna}$. **b** rising stage of the curve in the region marked by a rectangle in Fig. 8.16a

the loops in such correlation plots are caused by time delay between response at the points and/or by the stored water between both points, which becomes the sole reason when both points are fully hydraulically connected. In this case, the additional flow of the stored water results in slower recession at the downstream point, as compared to the upstream point. Larger floods may store more water between the points, which makes their hysteresis larger, as can be seen in Fig. 8.15a.

Note that the rate of head rise at P_1 becomes higher compared to the rate at P_2, when it is reached by back-flooding. The reason for this is that there are several conduits between both points that become pressurized when back-flooded, resulting in a large head-drop along them.

8.3.1.4 SWMM Model of the Hydraulic Response to High Recharge Event

We have modelled flood propagation through Škocjan Cave and Kačna Cave with SWMM. The model is based on the one presented by Gabrovšek et al. (2018), but only the first part of the system, relevant for P_1 and P_2, is taken and optimized manually. The plan view of the model is shown in Fig. 8.16a and the cross-section at different flood stages in Fig. 8.16c. Figure 8.16b shows observed and measured response at P_1 and P_2 during the period of the February 2009 flood. Despite the fact that the model's geometry is highly simplified and partially unknown, the model captures all characteristics of the observations. Four stages of the flood event are shown in Fig. 8.16c(1–4):

- before the flood, when all the water is drained by the low water sump beyond P_2 (Fig. 8.16c1);
- when overflow is active and P_2 is already back-flooded, but the response at P_1 is still small (Fig. 8.16c2);
- at the peak, where all conduits are pressurized (Fig. 8.16c3); and
- when P_1 has dropped almost to base level and P_2 is still high (Fig. 8.16c4).

8.3.1.5 Flood Event in February 2019

Between 27 January and 4 February 2019, over 300 mm (almost 200 mm in the most intensive 30 h period) of rain fell in the mountainous region of Mt. Snežnik and about 150 mm in the area of Škocjan. The discharge of the Reka River at the Cerkvenikov Mlin gaging station peaked at 300 m^3/s. During the event the water in Škocjan Caves rose at rates up to 10 m/h and reached a level of 305 m a.s.l. in Martel's Chamber (Figs. 8.17 and 8.18) and about 307.5 m a.s.l. in Šumeča Jama. The flood was the largest in the last 50 years. High water caused severe damage to infrastructure and deposited a considerable amount of mud; at some places the thickness of fresh deposits was above 50 cm (Fig. 8.19).

8.3.2 Ljubljanica River Recharge Area

The Ljubljanica River Recharge area is an over 1600 km^2 large karstic catchment in central Slovenia. The regional groundwater flow is governed by complex structures comprising thrusts and large fault zones. The most dominant of the latter is the Idrija Fault Zone (IFZ), which crosses the area in a SE–NW direction and acts as a barrier for groundwater flowing from the mountainous regions of the South, towards the Ljubljana Basin at the north. Along the Idrija Fault Zone a cascading set of karst poljes with overland flow has formed. Poljes exchange water with the surrounding karst massifs via springs, ponors and estavelas.

We present a selection of results based on observations in caves and ponors between Planinsko Polje, and the springs of the Ljubljanica River near Vrhnika, at the rim of the Ljubljana Basin (Fig. 8.20). Planinsko Polje is the NW-most of the active poljes formed along the Idrija Fault Zone. It is an overflow polje with main springs on its southern side, gathering waters from higher positioned poljes and mountainous areas to the south. The springs merge into the Unica River (Q_{min} = 1.1 m^3/s, Q_{av} = 21 m^3/s, Q_{max} > 100 m^3/s) with almost 17 km of flow length along the 5 km long polje. After about 5 km of flow the river approaches the border of the polje and loses most of its low to medium flow along the Eastern Ponor Zone (Blatnik et al. 2017). During floods, the limiting capacity and/or back-flooding of the Eastern Ponor Zone diverts the excess of flow towards the ponor zone at the northern border of the Polje. When the recharge exceeds about 60 m^3/s, the Polje starts to flood. During the highest floods, up to 100 × 10^6 m^3 of water can be stored in the Polje.

The results presented in this chapter are based on three years of observations in ponors P_1–P_3 and caves E_1, E_2, W_1–W_3, H_1 and H_2 (Fig. 8.20). Detailed results and descriptions of the methods are given in Blatnik et al. (2019). The flow system adjacent to Planinsko Polje is extremely complex and intertwined; however, Blatnik et al. (2019) have shown that the main characteristics of groundwater dynamics can be explained with the basic principles given above and simulated with relatively simple SWMM models. Here we present some examples.

Based on the past research, the area can be divided into the three subsystems, which are shown in Fig. 8.20:

- the system related to the Eastern Ponor Zone (P_1–E_1–E_2),
- the system linked to the Northern Ponor Zone (P_2, P_3–W_1–W_2–W_3), and
- the system related to flow from the Hrušica Plateau (P_2*, H_1, H_2).

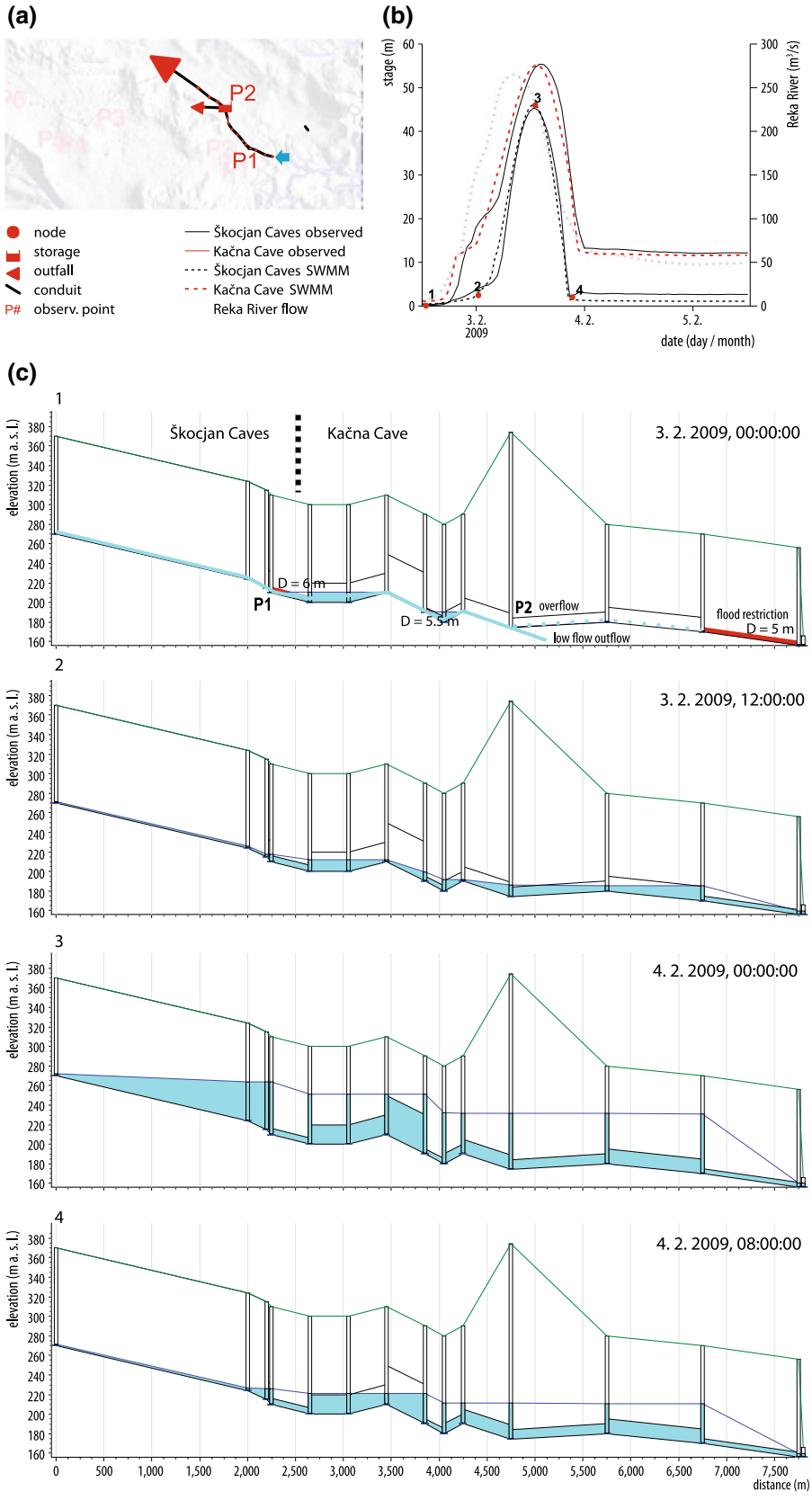

Fig. 8.16 **a** Plan view of the SWMM model; **b** modelled (dashed lines) and observed (full lines) responses at P_1 and P_2 during the flood event in February 2009. The recharge is shown by grey dotted line. Points 1–4 show four positions of stages presented in Fig. 8.16c; **c** cross-section of the model at four stages during flood event (see the text in the Sect. 8.1.3.4. Pale blue regions denote the water level, green lines show total had along the profile

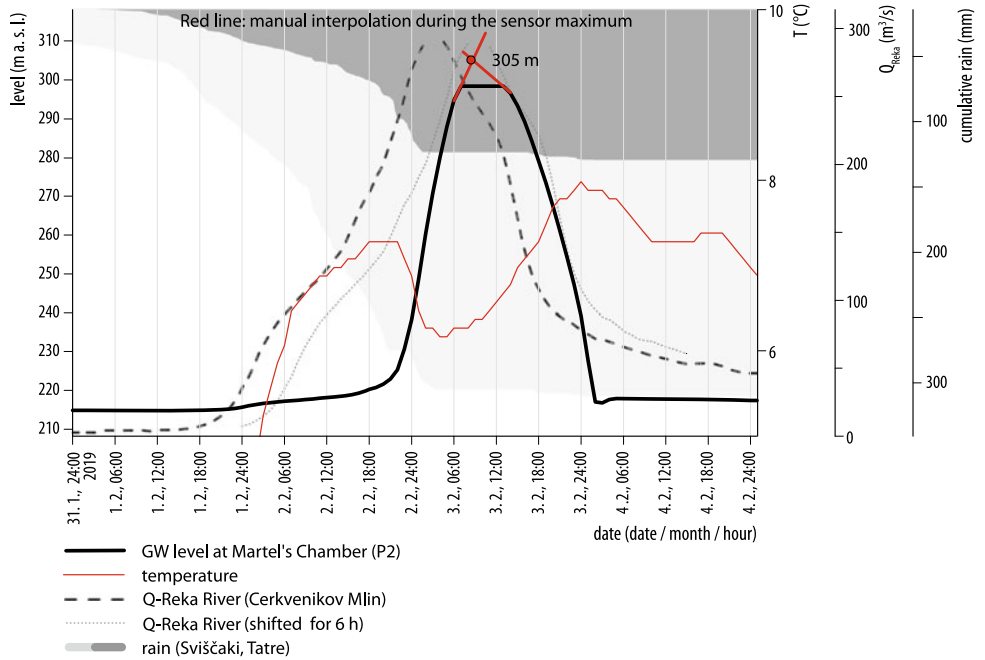

Fig. 8.17 The flood event of 2019: cumulative rain at two stations, discharge of the Reka River and level and temperature in Martel's Chamber. Dotted grey line shows discharge shifted for six hours, an estimated travel time from gaging station to Martel's Chamber

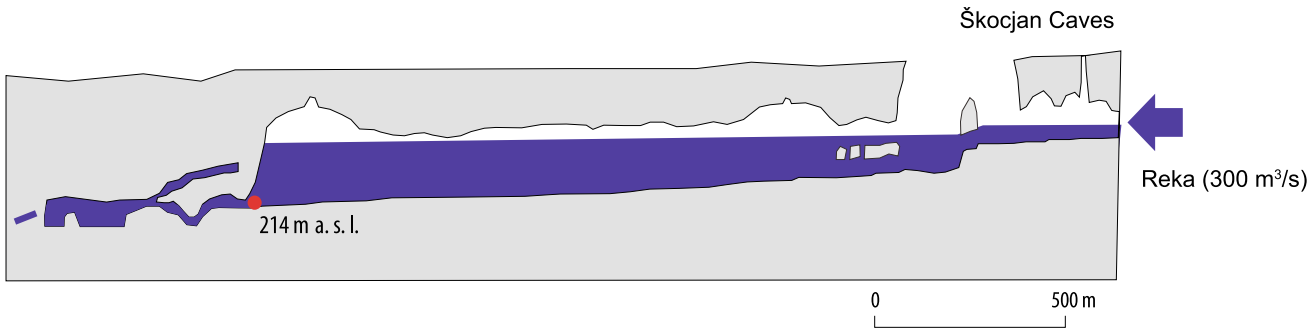

Fig. 8.18 A simplified extended elevation of Škocjan Caves with approximate maximal water level during the flood of February 2019

Figure 8.21 shows levels at P_1, E_1 and E_2 in February 2017. The observation point E_1 is in a shaft connecting the base flow conduits to an overflow channel. The observation point at E_2 is close to the inflow sump. The connection between E_1 and E_2 is not explored, but the data indicate very good hydraulic connectivity between the points (Fig. 8.21). Note that the level drop between the Polje (P_1) and E_1 is much smaller than between E_1 and E_2, indicating that the back-flooding of the ponors is caused by the limiting transmissivity of the conduit system, deeper in the aquifer.

At E_1, the most evident inflection point corresponds to the position of a major overflow channel at 440 m a.s.l. Correlation of heads at E_1 and E_2 shows similar hysteresis at all major flood events (Fig. 8.22). During the rising stage, the head at E_1 initially rises rapidly until the overflow passage at 440 m a.s.l. is reached. The head at E_1 is then bound to the position of the overflow, while rapid increase continues at E_2 due to active overflow. Further head increase at both points is controlled by restriction beyond E_2, where both points and the overflow are back-flooded. The recession at both points

Fig. 8.19 Photos of the 2019 flood: **a** Velika Dolina collapse valley; **b**, **c** Šumeča Jama (Rumouring Cave); **d** flood deposits on the footpath in Hanke's Channel

initially follows the rise, but then deviates from the rising curve. Blatnik et al. (2019) proposed a model, which includes relatively large storage in the overflow passage (Fig. 8.23). During the recession, the inflow of the stored water prevents head-drop at E_2. The concept was tested by a SWMM model, which produced hysteresis in the correlation plot if the overflow conduit between E_1 and E_2 had considerable storage (Fig. 8.22b).

Similar principles, tested by SWMM models, were used by Blatnik et al. (2019) to analyse hydrographs from the other two subsystems delineated in Fig. 8.20. In the subsystem related to the northern ponors (P_2, P_3, W_1–W_3), the flow from ponor zone P_2 bypasses the nearest cave W_1 and feeds directly the region of W_2–W_3. When the ponor zone P_2 is back-flooded, the flow in the polje is re-routed to higher positioned channels leading to P_3, which then triggers fast response at W_1. The concept is shown in Fig. 8.24.

They also identified several overflow levels between W_1–W_2–W_3. Some of these were expected from the cave surveys, some were unexpected (Fig. 8.25). Blatnik et al. (2019) also introduced a plot, where rate of water rise/drop is plotted against the head. As expected, the rate show minima at the positions of overflow conduits (Fig. 8.26).

System H_1–H_2 receives autogenic recharge from the region of the Hrušica Plateau to the south and from the mixed recharge of the Hotenjka region to the west. H_1 and H_2 are on the opposite (SW) side of Idrija Fault Zone with respect to other observation points (E_1–E_2, W_1–W_3). H_1 is a simple shaft, reaching a very stagnant water level and H_2 is a shaft, which becomes partially flooded during high water events. During high water events (Blatnik et al. 2019), the level in the region of H_1 and H_2 increases rapidly and the region discharges to the NW side of Planinsko Polje. The level at H_1 and H_2 also recedes fast and the water flows from

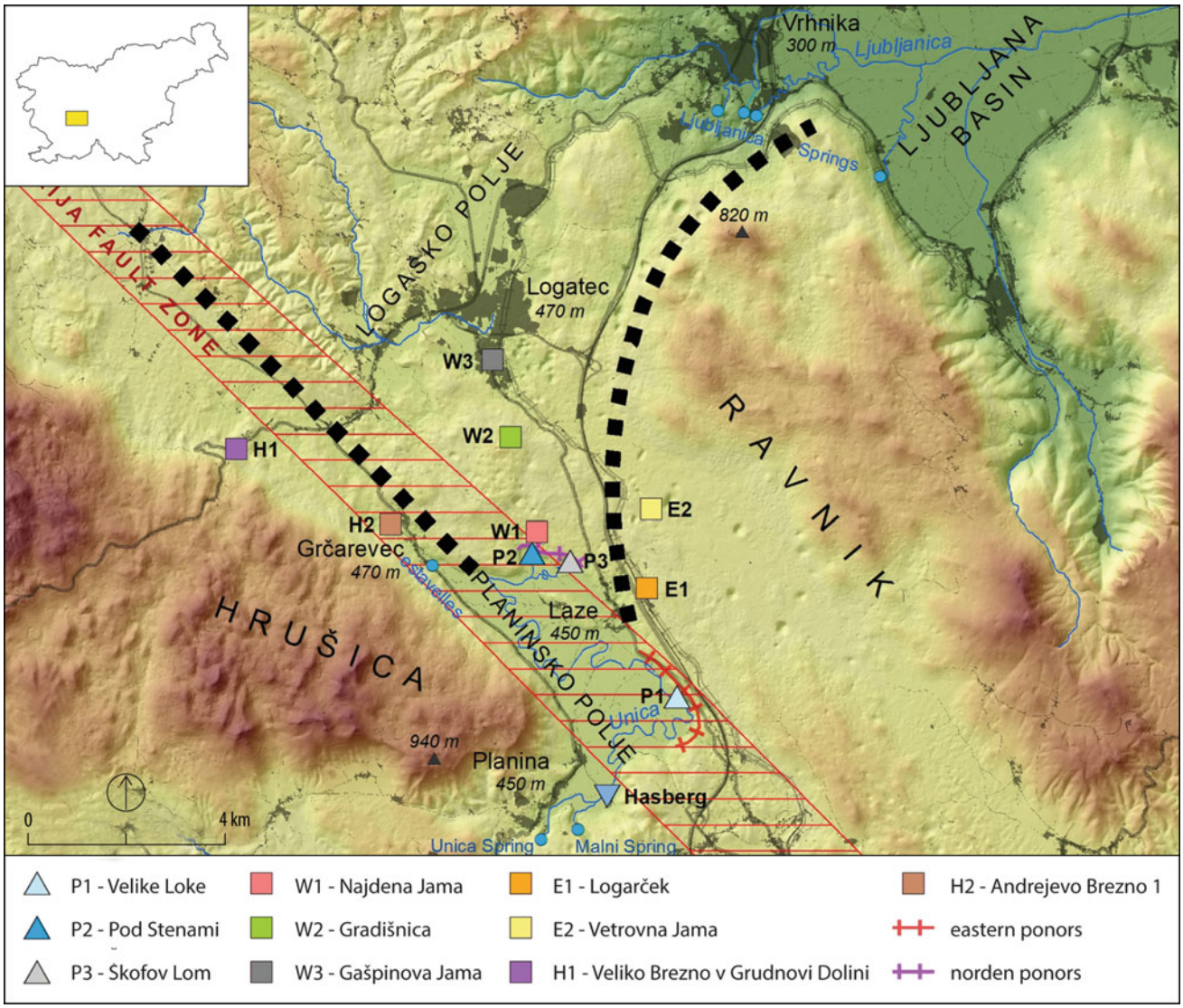

Fig. 8.20 The area between Planinsko Polje and Ljubljanica Springs, showing all observation points: monitored ponors (triangles) and water caves (squares). The dashed lines delineate flow systems; see text for discussion

the flooded polje into the region of H_1–H_2. The hydrographs at H_1 also indicate a high transmissivity level in the Idrija Fault Zone, which keeps a very stable water level at H_2. During floods, the area of H_1–H_2 seems to be back-flooded due to constrictions along the flow paths on the down-flow side of the Idrija Fault Zone.

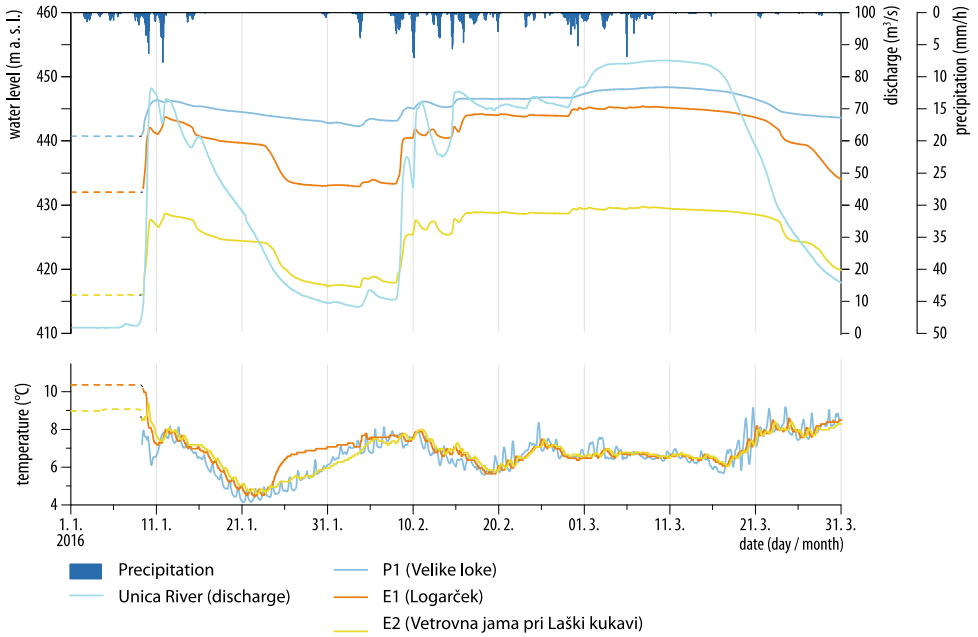

Fig. 8.21 Levels (upper panel) and temperatures (lower panel) at P_1, E_1 and E_2 and flow rates of the Unica River during winter 2016

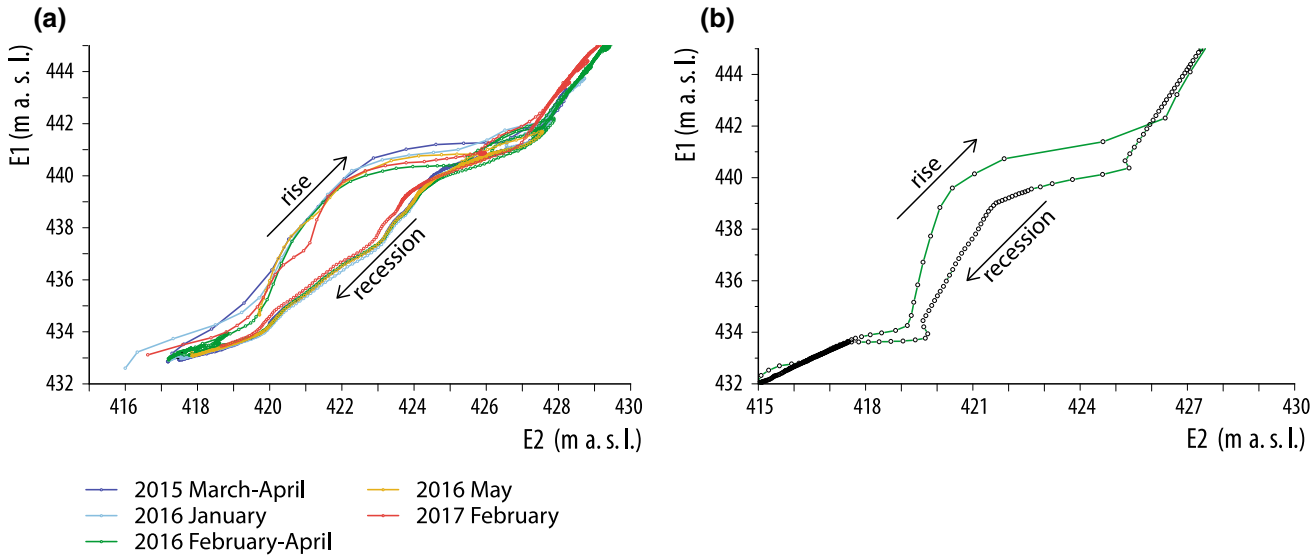

Fig. 8.22 Correlation between heads at observation points in E_1 and E_2: **a** measurements during several high water events; **b** results of a modelled event, with hysteresis indicating storage between the two observation points

Fig. 8.23 SWMM model of the system P_1, E_1, and E_2 at high water

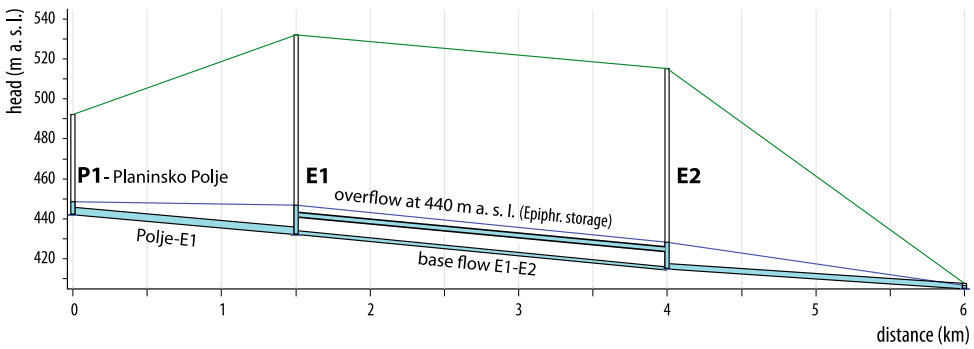

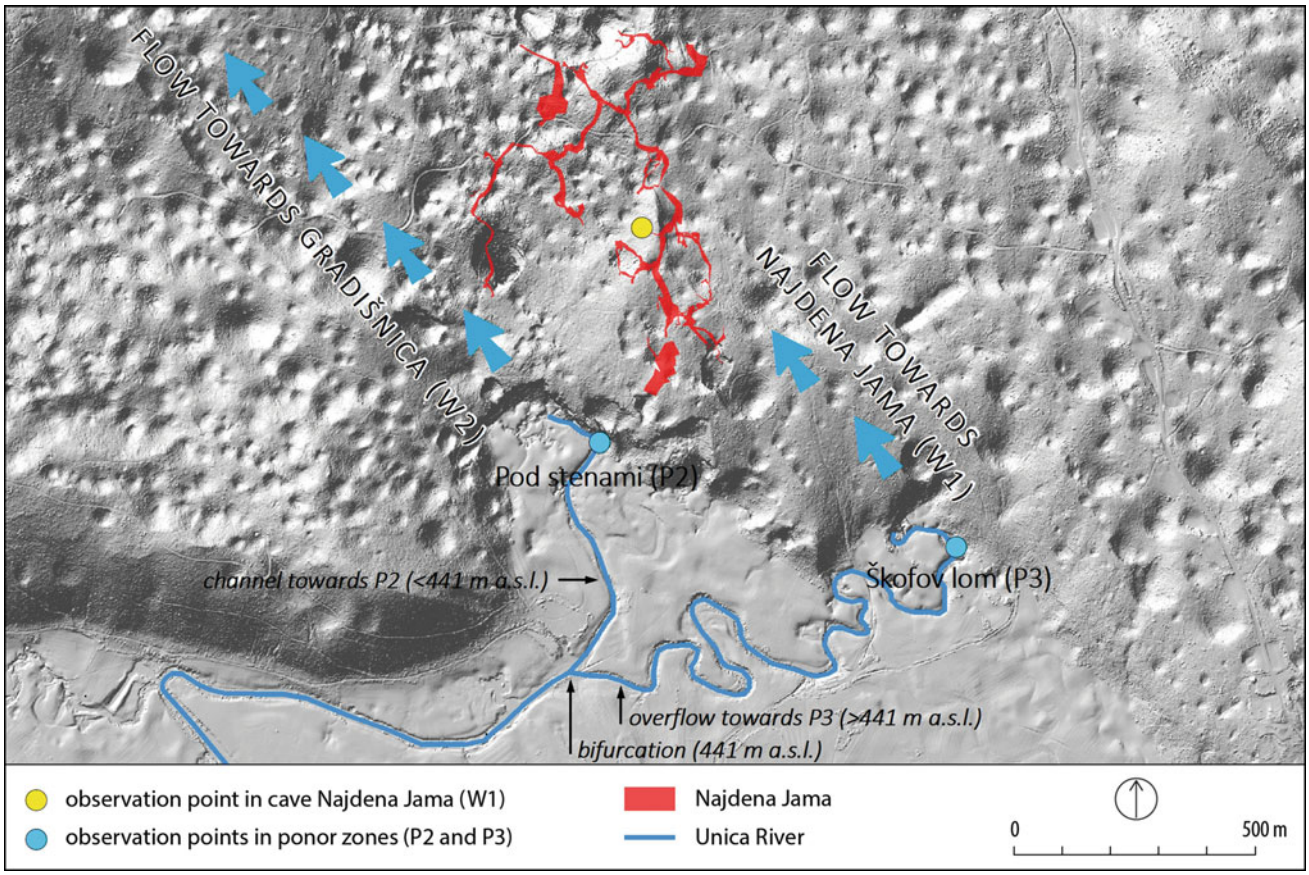

Fig. 8.24 Northern border of Planinsko Polje with ponor zones P_1 and P_2, Najdena Jama (W_1) and inferred flow directions. The back-flooding of P_2 diverts the flow on the polje towards P_3, which is followed by a fast response at W_1. From Blatnik et al. (2019)

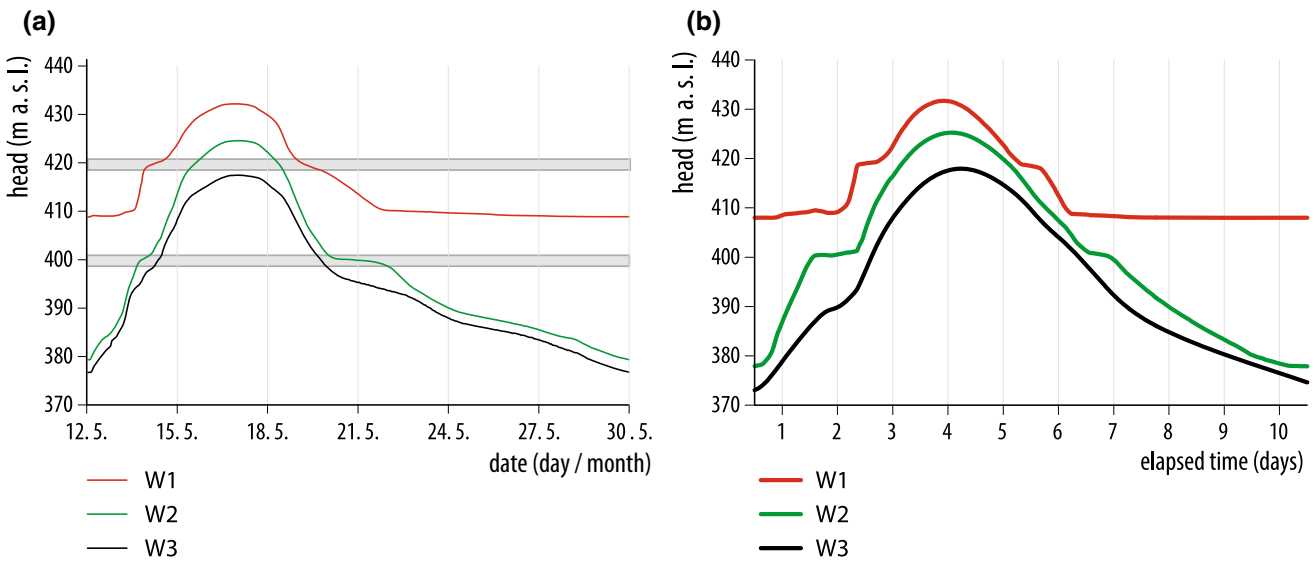

Fig. 8.25 **a** Level hydrographs at W_1–W_3 during a flood event in May 2016. Grey lines denote positions of overflow; **b** hydrographs obtained from SWMM model of conduit system between P_2, P_3 and W_1–W_3. From Blatnik et al. (2019)

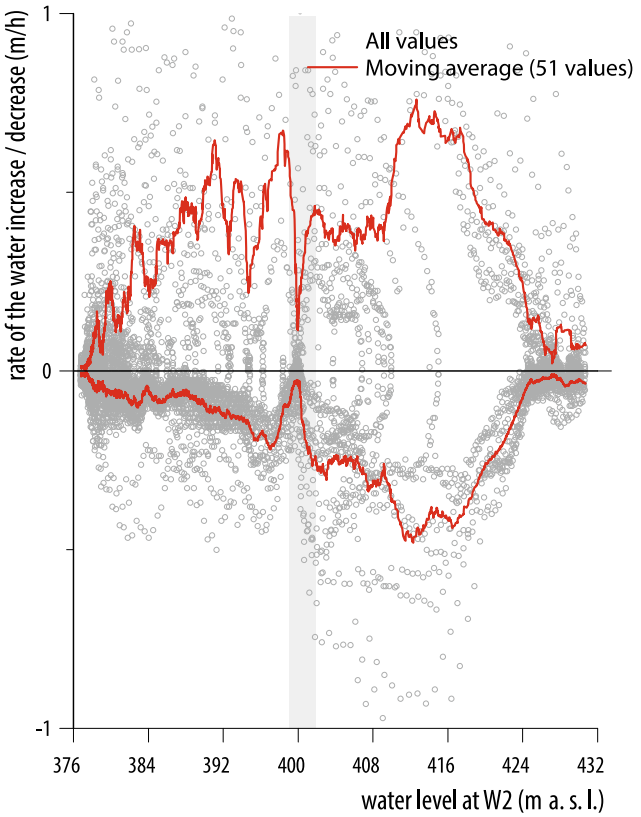

Fig. 8.26 Rate of head increase/decrease at W_2 shows a clear minimum at the overflow position at 400 m a.s.l. This corresponds to the inflection marked in Fig. 8.25a and to the position of the known existing channel

8.4 Conclusion

Several other studies in the Dinaric Karst demonstrated the power of combining observations in cave systems and hydraulic modelling to understand the function of a karst aquifer. Kaufmann et al. (2016) used the approach to analyze the observations at six stations positioned along the underground flow of the Pivka River in Postojna Cave. They employed a survey of the conduit system as an initial geometry, which was further constrained by an optimization procedure resulting in an excellent fit of the observed data. A recent ongoing study is examining the springs of Planinsko Polje. There, an interesting distribution of flow between the two main springs seems to be controlled by an overflow over a breakdown zone in the region of Planinska Jama, where two main inflows merge into a lake and then diverge towards base flow and overflow springs. Kaufmann et al. (2019) tested this hypothesis using the known geometry of the conduit system and SWMM model, optimized to fit the archival data of flow rates of springs and contributing ponors. Ongoing research also includes observations within the system and will provide more details on the mechanisms involved.

In this chapter most of the discussion was focused to the level hydrographs, although temperature, specific electric conductivity and/or other observed parameters may give us further insights into the system, such as travel time estimation between points, onset and cessation of overflow mechanism, etc. Examples from the Dinaric karst are given in Gabrovšek et al. (2018), Covington et al. (2011), and Blatnik et al. (2019).

Due to remoteness and difficult accessibility, caves have been rather overlooked as observation points within karst aquifers. However, as shown by recent studies, observation of epiphreatic flow at multiple access points combined with hydraulic modelling offers new insights into the structure and mechanism of hydraulic processes in the karst conduit systems. The importance of good cave surveys, which enable building of the initial models and give constraints to the final model applied, is paramount. Therefore, the volunteering and enthusiastic work of cavers is highly appreciated.

It is also important to stress that models which give a good qualitative or quantitative fit to the observed data do not necessarily represent what is actually present in nature (i.e. unique solutions). However, they do provide a physically based explanation of what may be there or why the hydrographs have a given shape.

Additional theoretical work is needed to obtain better data processing and automatic identification of features and mechanisms. Another interesting question is how much information about the phreatic zone is hidden in the data.

References

Audra P, Palmer AN (2013) The vertical dimension of karst: controls of vertical cave pattern. In: Shroder JF (ed) Treatise on geomorphology 6. Academic Press, San Diego, California, pp 186–206

Blatnik M, Frantar P, Kosec D, Gabrovšek F (2017) Measurements of the outflow along the eastern border of Planinsko Polje, Slovenia. Acta Carsolog 47(1):83–93

Blatnik M, Gabrovšek F, Mayaud C (2019) Groundwater dynamics between Planinsko Polje and springs of the Ljubljanica River, Slovenia. Acta Carsolog 48(2):199–226

Chen Z, Goldscheider N (2014) Modeling spatially and temporally varied hydraulic behavior of a folded karst system with dominant conduit drainage at catchment scale, Hochifen-Gottesacker, Alps. J Hydrol 514:41–52

Chow VT (1988) Open-channel hydraulics. McGraw-Hill, New York

Covington MD, Luhmann AJ, Gabrovšek F, Saar MO, Wicks CM (2011) Mechanisms of heat exchange between water and rock in karst conduits. Water Resour Res 47(10):W10514

Dingman SL (2002) Physical hydrology. Prentice Hall, Upper Saddle River, N.J.

EPA U (2014) Storm water management model (SWMM). US Environmental Protection Agency. http://www.epa.gov/nrmrl/wswrd/wq/models/swmm/

Ford DC, Williams PW (2007) Karst hydrogeology and geomorphology. Wiley, Chichester, p 562

Gabrovšek F, Peric B (2006) Monitoring the flood pulses in the epiphreatic zone of karst aquifers: the case of Reka river system, Karst plateau, SW Slovenia. Acta Carsolog 35(1):35–45

Gabrovšek F, Häuselmann P, Audra P (2014) 'Looping caves' versus 'water table caves': the role of base-level changes and recharge variations in cave development. Geomorphology 204:683–691

Gabrovšek F, Peric B, Kaufmann G (2018) Hydraulics of epiphreatic flow of a karst aquifer. J Hydrol 560:56–74

Jeannin P (2001) Modeling flow in phreatic and epiphreatic karst conduits in the Holloch cave (Muotatal, Switzerland). Water Resour Res 37(2):191–200

Kaufmann G, Gabrovšek F, Turk J (2016) Modelling cave flow hydraulics in Postojnska jama, Slovenia. Acta Carsolog 45(1): 57–70

Kaufmann G, Mayaud C, Kogovšek J, Gabrovšek F (2019) Understanding the temporal variation of flow direction in a complex karst system Planinska jama, Slovenia. Acta Carsolog (in press)

Peterson E, Wicks C (2006) Assessing the importance of conduit geometry and physical parameters in karst systems using the storm water management model (SWMM). J Hydrol 329(1–2):294–305

Rossman LA (2009) Storm water management model, Version 5.0. US Environmental Protection Agency, Cincinnati

Rozos E, Koutsoyiannis D (2006) A multicell karstic aquifer model with alternative flow equations. J Hydrol 325(1–4):340–355

Šebela S (2009) Structural geology of the Škocjan Caves (Slovenija). Acta Carsolog 38(2–3):165–177

Vuilleumier C (2019) Hydraulics and sedimentary processes in the karst aquifer of Milandre (Jura Mountains, Switzerland). University of Neuchatel, Neuchatel